Build Optimization of Fiber Reinforced 3D-Printed Components

Aaditya Chandrasekhar   Tej Kumar   Krishnan Suresh

achandrasek3@wisc.edu   tkumar3@wisc.edu   ksuresh@wisc.edu

Abstract

Additive manufacturing has enabled component fabrication with unprecedented geometric and material complexity. The focus of this paper is on the AM build optimization of short fiber reinforced polymers (SFRP) components. Specifically, we consider optimization of the build direction, infill pattern and fiber orientation. All three factors have a significant impact on the functional performance of the printed part, and significant progress has been made on optimizing these independently. The objective of this paper is to consider all three factors simultaneously, and explore their interdependency, within the context of thermal applications.

Towards this end, the underlying design parameters are identified, and a formal optimization problem is posed, as an extension to the popular Solid Isotropic Material with Penalization (SIMP). Appropriate sensitivity equations are derived, and an assembly-free finite element analysis is formulated. Results from several numerical experiments are presented, highlighting the impact of build direction, infill topology and fiber orientation on the performance of SFRP components.

1   Introduction

Additive manufacturing (AM) has opened new opportunities to create parts with unprecedented geometric and material complexity. In AM, components are fabricated layer-by-layer, as opposed to a subtractive process [15]. Fused deposition modeling (FDM) is one such AM process where a continuous thermoplastic (polymer) filament is deposited layer-by-layer (see Figure 1(a)). With continuously improving materials and fabrication technology, FDM is being used today to make functional parts for thermal and structural applications. For example, Figure 1(b) illustrates a heat exchanger where FDM's process capabilities are exploited to achieve large surface to volume ratio. Further, in such applications, to enhance performance, the polymer is often infused with short (typically, carbon) fibers [3] (Figure 1(c)).The functional properties of such short fiber reinforced polymers (SFRP) components depend significantly on the fiber distribution and orientation. These can be controlled in FDM by suitability modifying the raster path. Finally, to reduce print time and material usage, the interior of such SFRP components is made porous via a suitable infill pattern (Figure 1(d)).

The focus of this paper is on the build optimization of SFRP components. Specifically, the objective is to optimize the build direction, the infill pattern and fiber orientation (raster path) for thermal applications (Figure 2). While significant progress has been made on each of these topics (for example, see [2] and [12]), the objective here is to consider all three factors simultaneously.

Towards this end, the remainder of this paper is organized as follows.The literature review is carried out in Section 2. This is followed by a discussion on problem formulation in Section 3. Results are discussed in Section 4, with a concluding note in Section 5.

(a) Illustration of the fused deposition modeling [37].

(b) A heat exchanger is printed using Carbon fiber reinforcement. This illustrates some of the recent advances in AM to print functional components. The image portrays the infill strategy used and the presence of fiber reinforcement in the polymer matrix.

(c) Polymers are filled with fibers to enhance mechanical properties [42]

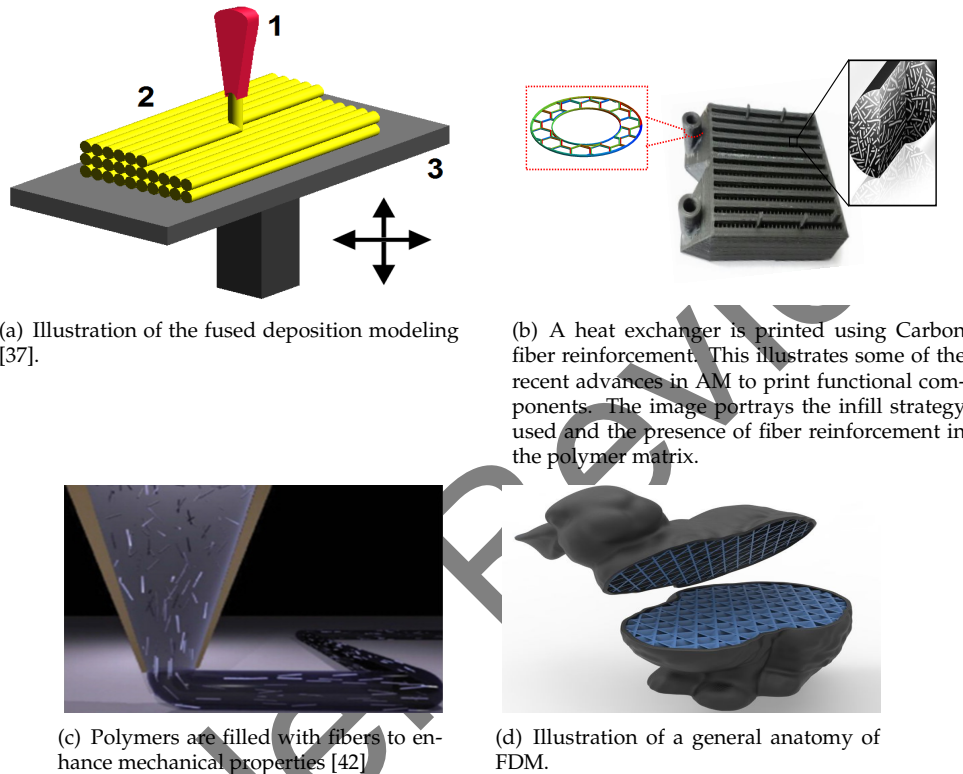(d) Illustration of a general anatomy of FDM.

Figure 1: Fused Deposition Modeling of Fiber-Filled Composites.
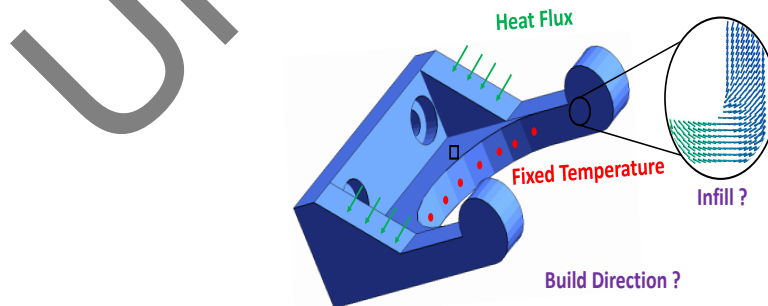

Figure 2: An SFRP component (wall mount) subject to thermal loading; the optimal build direction, infill topology and fiber orientation must be determined.

2 Literature Review

As discussed in the previous section, the objective here is to compute the optimal *build direction*, the *infill topology* and *fiber orientation*, to improve functional performance of SFRP parts. Prior work related to the above three build parameters is discussed next.

2.1 Build Direction

The build direction plays a significant role in the surface quality, print-time, and sacrificial support of FDM components; see [2], [8],[27], [23], [25]. This paper focuses on the interplay between build direction and functional performance of the part. For example, it is well known FDM introduces behavioral anisotropy [21], primarily due to incomplete fusion adjoint layers. Umetani [36] proposed a structural analysis technique based on a bending moment concept to optimize the build direction; however, isotropic material was assumed for simplicity, i.e., fiber reinforcement was not considered. On the other hand, material anisotropy was considered by Erva [35] where the build direction was optimized to maximize structural safety factor using a surrogate-optimization model; but, infill topology was not considered.

2.2 Infill Topology

A porous infill topology reduces material usage and print time. Optimized infill patterns have been considered by several authors. Martinez [20] proposed a stochastic method to generate compliant structures with a voronoi infill. Steuben [33] proposed a implicit slicing method to produce components with tailored functional properties. Recently, Chougrani [6] suggested a lattice infill for AM. Wu et al. [38] proposed a global optimization framework to generate bone-like porous infill. They also proposed a two-scale simultaneous optimization of shell-infill in the context of minimizing structural compliance [39]. Recently, Dapogny [7] performed a 2D topology optimization considering specific infill patterns with anisotropic behavior. The limitation of prior work is that they assume a pre-defined build direction, and associated anisotropy.

2.3 Fiber Orientation

The problem of optimizing fiber orientation angle has been addressed within the context laminar composites. Discrete material optimization (DMO) is one of the most popular approaches, where a list of a priori directions (eg $0°, \pm 45°, \pm 90°$) [32] is used. This avoids local minima, but can result in sub-optimal results. Interpolation schemes have also been suggested to overcome this limitation. Alternately, continuous fiber angle optimization (CFAO) has also been proposed [4]. This offers greater design freedom, but can result in a local minima. While the focus has been on laminar composites, there has been a recent increase in targeting these methodologies for AM. For example, Brenken [5] recently observed that fibers orient preferentially in the direction of extrusion of the filament from the print-nozzle, which provides a larger degree of control in the material properties of the fabricated part. They also concluded that the effect of a layer-wise printing strategy

combined with the preferential orientation of the fibers results in a complex mechanical behavior.

2.4 Paper Contributions

The main contribution of this paper is a *comprehensive* approach to the build optimization of thermally loaded SFRP components by simultaneously considering the impact of build direction, infill topology and fiber orientation. In particular, the current work extends the popular Solid Isotropic Material with Penalization (SIMP) method [30]. The specific contributions are:

1. A formulation to obtain infill pattern, density and build direction for anisotropic FDM components based on structural optimization.

2. An assembly-free finite element framework to analyze large scale structured mesh for heat conduction problems with an emphasis on reducing memory footprint and hence computational cost.

3. A detailed parametric study on the obtained results to gain insights into the effects of build parameters.

3 Problem Formulation

We start by discussing the design variables used in our formulation. This leads to a discussion on the optimization problem and sensitivity analysis. We then discuss the proposed algorithm and the finite element solver.

3.1 Design Parameters

Build Direction

Due to the incomplete fusion between subsequent layers of deposited material, the thermal conductivity tends to be lower in the direction of the build, leading to transversely isotropic properties. Prajapati [26] proposed to model the effective thermal conductivity along the build direction via

$$\frac{1}{k_z} = \frac{w_a + w_f}{w_a k_a + w_f k_f} + \frac{R_c}{L_h} \tag{1}$$

where k_z is the thermal conductivity in the build direction, k_a is the thermal conductivity of air, k_f is the thermal conductivity of the filament (with no fiber reinforcement), w_a is the air-gap between rasters, w_f is the width of the raster. R_c is the contact resistance between adjacent layers and L_h is the layer height. Experimental studies show R_c to be in the order of $500 - 2000$ $[\mu K m^2 W^{-1}]$ leading to $k_z/k_f \approx 0.6 - 0.8$. Similar decrease in mechanical properties have been reported by Knoop [17] and Farzadi [11]. Observe that build-direction anistropy is different from fiber induced anisotropy [42].

In our formulation, we assume the part to have an initial build direction along the global Z-axis. We introduce *two* design parameters α_0 and β_0 as Eulerian angles to capture the rotation of the build direction about the global X and Y axis respectively via Equation 2. These two angle parameters are to be determined by the optimizer.

$$\vec{b} = R_x(\alpha_0)R_y(\beta_0)\vec{z} \tag{2}$$

where R_x and R_y are standard rotation matrices.

Fiber Orientation

Next, we consider anisotropy due to fiber infill. Mulholland [24] reported thermal anisotropy of specific SFRP materials (see Table1). Here $k_{\parallel}$ is the thermal conductivity achieved along the principal direction of the fibers, levaraging their higher conductivity and $k_{\perp}$ can be attributed as the thermal conductivity imparted by the filament matrix. Since $k_{\perp}/k_{\parallel} \approx 0.13 - 0.38$, it is important to orient the fibers in an optimal fashion. As observed in [5], fibers tend to orient along the direction of travel of the extrudate. This will be compounded by the build direction induced anisotropy.

Material	$k_{\parallel}$ [W/m-K]	$k_{\perp}$ [W/m-K]
Onyx	0.88	0.30
PA6-CuF-20	4.84	0.76
PA6-CuF-25	5.52	0.77
RTP 0299 X 137152 C NAT/BLK	5.00	1.50
RTP 0299 X 137077 C NAT/BLK	18.01	4.50

Table 1: Thermal Conductivity of Some SFRPs used in Fused Filament Fabrication

The finite element formulation used here (see later section) utilizes a geometrically congruent hexahedral (voxel) mesh. Thus, every finite element e is assigned an orientation angle θ_e, on a plane perpendicular to the build direction. This angle will be determined by the optimizer. The resulting conductivity matrix can be expressed as:

$$[K]_e = R_{\vec{b}}(\theta_e)\hat{K}R_{\vec{b}}^T(\theta_e) \tag{3}$$

$$[\hat{K}] = \begin{bmatrix} k_{\parallel} & 0 & 0 \\ 0 & k_{\perp} & 0 \\ 0 & 0 & k_z \end{bmatrix} \tag{4}$$

where $[\hat{K}]$ is the thermal conductivity matrix along the principal directions assumed to be coincident with the global coordinates of the model. Combining the anisotropy due to layer-wise build (as discussed in the previous section) with that imparted by the fibers, we can see that $k_z/k_{\parallel} \approx 0.08 - 0.31$. Further, $[R_{\vec{b}}(\theta_e)]$ expresses the orientation of the infill fiber material with respect to the build direction.

5

Infill Topology

Next we consider the parameterization of infill topology. Here, the evolution of the topology is modeled using classic SIMP where each finite element e is assigned a density value $\rho_e \in [0, 1]$. A density value of one denotes the presence of material, and zero its absence. The density is further penalized by a constant p relating the material property via a power-law:

$$[k]_e = [k_0] + \rho_e^p (R(\alpha_0, \beta_0, \theta_e)([\hat{k}] - [k_0])R(\alpha_0, \beta_0, \theta_e)^T) \tag{5}$$

where $[k_0]$ is a small thermal conductivity assigned to empty voxels to prevent singularities in the solver. We penalize the model with $p = 3$. The rotation matrix is given by:

$$R(\alpha_0, \beta_0, \theta_e) = \begin{bmatrix} 1 & 0 & 0 \\ 0 & \cos(\alpha_0) & -\sin(\alpha_0) \\ 0 & \sin(\alpha_0) & \cos(\alpha_0) \end{bmatrix} \begin{bmatrix} \cos(\beta_0) & 0 & \sin(\beta_0) \\ 0 & 1 & 0 \\ -\sin(\beta_0) & 0 & \cos(\beta_0) \end{bmatrix} \begin{bmatrix} \cos(\theta_e) & -\sin(\theta_e) & 0 \\ \sin(\theta_e) & \cos(\theta_e) & 0 \\ 0 & 0 & 1 \end{bmatrix} \tag{6}$$

Observe that Equation 5 combines the effect of build direction (α_0 and β_0), fiber orientation (θ_e) and infill density (ρ_e), resulting in $2n + 2$ degrees of freedom where n is the number of finite elements.

3.2 Optimization Formulation

We are now ready to consider the optimization problem. For a typical thermal problem (example: see Figure 2), our objective is to minimize the thermal compliance (see Gersborg [14], Gao [13], Li [19], [10]). Here we rely on topology optimization (TO) [1], [31], [9]) where thermal compliance C is defined as in equation 7 with Θ being the temperature and f being the imposed heat load.

Observe that we have imposed a global volume constraint on the domain (Equation 8), where v_e is the volume of the mesh element and V_f is the desired volume fraction. The behavior of the system is governed by a system of algebraic equations (9) derived from the finite element discretization of a steady state heat conduction problem. $[K]$ is the stiffness matrix, $\{\Theta\}$ is the temperature field and $\{f\}$ is the external heat applied. The constraints for the build orientation is given by Equation 10 and 11. The constraint for fiber orientation is given by Equation 12 and Equation 13 sets the limit for density.

$$\min_{\Omega \subset \Omega_0} \quad C = \int_\Omega f\Theta d\Omega = \{f\}^T\{\Theta\} \tag{7}$$

$$\text{s.t.} \quad g(\rho) \equiv \frac{\sum\limits_e \rho_e v_e}{V_f \sum\limits_e v_e} - 1 \le 0 \tag{8}$$

$$[K]\{\Theta\} = \{f\} \tag{9}$$

$$\alpha_0 \in [0, 2\pi] \tag{10}$$

$$\beta_0 \in [0, 2\pi] \tag{11}$$

$$\theta_e \in [0, \pi] \quad \forall e \tag{12}$$

$$\rho_e \in [0, 1] \quad \forall e \tag{13}$$

3.3 Sensitivity Analysis

In order to perform gradient based optimization, the sensitivity of the objective and constraints, with respect to the design variables is derived in this section.

Objective Sensitivity

Recall that the thermal compliance is given by:

$$\mathcal{C} = \{f\}^T\{\Theta\} \equiv \{\Theta\}^T[K]\{\Theta\} \tag{14}$$

Differentiating equation (14) with respect to a generic design variable x_i, we have,

$$\frac{\partial\{\mathcal{C}\}}{\partial x_i} = \frac{\partial\{\Theta\}}{\partial x_i}^T[K]\{\Theta\} + \{\Theta\}^T\frac{\partial[K]}{\partial x_i}\{\Theta\} + \{\Theta\}^T[K]\frac{\partial\{\Theta\}}{\partial x_i} \tag{15}$$

Neglecting design-dependent loads we have, $\frac{\partial f}{\partial x_i} = 0$, Equation (9) is differentiated with respect to design variable x_i to get,

$$\frac{\partial\{\Theta\}}{\partial x_i} = [K]^{-1}\frac{\partial[K]}{\partial x_i}\{\Theta\} \tag{16}$$

Inserting (16) into (17) results in:

$$\frac{\partial\{\mathcal{C}\}}{\partial x_i} = -\{\Theta\}^T\frac{\partial[K]}{\partial x_i}\{\Theta\} \tag{17}$$

In particular, we have

$$\frac{\partial[K]}{\partial\rho_e} = \iiint\limits_{\Omega_e} [B]^T\frac{\partial[k]_e}{\partial\rho_e}[B]d\Omega_e \tag{18}$$

where $[B]$ is the gradient of the shape function matrix and,

$$\frac{\partial[k]_e}{\partial\rho_e} = p\rho_e^{p-1}([R(\alpha_0,\beta_0,\theta_e)]([\hat{k}]-[k_0])[R(\alpha_0,\beta_0,\theta_e)]^T) \tag{19}$$

Similarly, the sensitivity with repect to θ_e is given by:

$$\frac{\partial[\boldsymbol{K}]}{\partial\theta_e} = \iiint\limits_{\Omega_e}[B]^T\frac{\partial[k]_e}{\partial\theta_e}[B]d\Omega_e \tag{20}$$

where,

$$\frac{\partial[k]_e}{\partial\theta_e} = \rho_e^p(\frac{\partial[R(\alpha_0,\beta_0,\theta_e)]}{\partial\theta_e}([\hat{k}]-[k_0])[R(\alpha_0,\beta_0,\theta_e)]^T + [R(\alpha_0,\beta_0,\theta_e)]([\hat{k}]-[k_0])\frac{\partial[R(\alpha_0,\beta_0,\theta_e)]^T}{\partial\theta_e}) \tag{21}$$

The sensitivity with respect to build orientation angle α_0 is given by,

$$\frac{\partial[\boldsymbol{K}]}{\partial\alpha_0} = \sum_e\iiint\limits_{\Omega_e}[B]^T\frac{\partial[k]_e}{\partial\alpha_0}[B]d\Omega_e \tag{22}$$

where $\frac{\partial[k]_e}{\partial\alpha_0}$ follows an expression similar to that of Equation 21. The sensitivity with β_0 follows suit with α_0 and is omitted here for sake of brevity.

Note that the sensitivity with respect to the build orientation angles (Equation 22) is summed over all elements. This is in contrast to sensitivity with respect to infill densities (Equation 19) and fiber orientation (Equation 20). In other words, build orientation is global, while infill density and fiber orientation apply to each element.

Constraint Sensitivity

The global volume constraint in Equation (8) can be expressed as

$$g(\rho) \equiv \frac{\sum\limits_e\rho_e v_e}{V_f\sum\limits_e v_e} - 1 \leq 0 \tag{23}$$

Thus,

$$\frac{\partial g}{\partial\rho_e} = \frac{v_e}{V_f\sum\limits_e v_e} \tag{24}$$

and the sensitivity is zero with respect to θ_e, α_0, and β_0. The box-constraints limiting the range of the design variables given by Equations 10, 11, 12 and 13 are considered implicitly by the globally convergent method of moving asymptotes (GCMMA) solver used in this paper [34]. The finite element solver is discussed in Section 3.5.

3.4 Optimization Algorithm

The optimization algorithm utilizes GCMMA [34], and is described below:

Algorithm 1 Build, Infill and Fiber Optimization

1: **procedure** BUILDOPT(V_c) $\triangleright$ Max. Vol. Frac. $V_c \in [0,1]$
2:      $i = 0$ $\triangleright$ Iteration Index
3:      $\phi = \{\bar{\rho}, \bar{\theta}, \alpha_0, \beta_0\}$ $\triangleright$ Opt. Variables
4:      $\Delta = 1.0$ $\triangleright$ Design Change
5:      **while** $\Delta > \epsilon$ and $i \leq$ MaxIter **do**
6:          $i \leftarrow i + 1$
7:          $[\boldsymbol{K}] \leftarrow (\phi)$ $\triangleright$ via Eq. 5
8:          $\{\boldsymbol{\Theta}\} \leftarrow [\boldsymbol{K}]^{-1}\{\boldsymbol{q}\}$ $\triangleright$ Deflated-Preconditioned Assembly-Free solver
9:          $\mathcal{C} \leftarrow (\{\boldsymbol{\Theta}\}, \{\boldsymbol{q}\})$ $\triangleright$ via Eq. 14
10:         $g \leftarrow (\bar{\rho}, V_c)$ $\triangleright$ Vol. Constraint Eq.8
11:         $(\frac{\partial \mathcal{C}}{\partial \rho_e}, \frac{\partial \mathcal{C}}{\partial \theta_e}, \frac{\partial \mathcal{C}}{\partial \alpha_0}, \frac{\partial \mathcal{C}}{\partial \beta_0}, \frac{\partial g}{\partial \rho_e})$ $\triangleright$ via Eq. 27,21,22, 24
12:         $\phi^i \leftarrow (\mathcal{C}, g, \frac{\partial \mathcal{C}}{\partial \rho_e}, \frac{\partial \mathcal{C}}{\partial \theta_e}, \frac{\partial \mathcal{C}}{\partial \alpha_0}, \frac{\partial \mathcal{C}}{\partial \beta_0}, \frac{\partial g}{\partial \rho_e})$ $\triangleright$ GCMMA Solver [34]
13:         $\Delta = (|\phi_e^i - \phi_e^{i-1}|)$

3.5 Assembly Free Finite Element Analysis

In classic finite element analysis, the element matrices are typically assembled into a global matrix, and solved during each step of the optimization process. In this paper, we will apply assembly-free FEA where the global stiffness matrix is neither assembled nor stored [40]. Instead, the fundamental matrix operations such as the sparse matrix-vector multiplication (SpMV) are performed in an assembly-free elemental level, i.e., an SpMV operation of $[K]\{u\}$ is interpreted as follows:

$$[K]\{u\} \equiv \sum_e ([K]_e\{u\}_e) \tag{25}$$

This idea was first proposed in 1983 [16], but has resurfaced due to the surge in fine-grain parallelization on multi-core frameworks. The technique reduces memory footprint leading to decreased computational cost, paving way for higher mesh resolution. It was shown in [18] how employing an assembly-free finite element solver may accelerate the convergence of AM simulation, entailing only entails minor modifications.

Consider the objective sensitivity in Equation (17) which can then be expressed as,

$$\frac{\partial \{\mathcal{C}\}}{\partial x_i} = -\{\boldsymbol{\Theta}\}^T \frac{\partial [\boldsymbol{K}]}{\partial x_i} \{\boldsymbol{\Theta}\} = -\sum_e \{\boldsymbol{\Theta}\}_e^T \frac{[\boldsymbol{K}]_e}{\partial x_i} \{\boldsymbol{\Theta}\}_e \tag{26}$$

In particular, the sensitivity with respect to density becomes,

$$\frac{\partial \{\mathcal{C}\}}{\partial \rho_e} = -\sum_e \{\boldsymbol{\Theta}\}_e^T \frac{\partial [\boldsymbol{K}]_e}{\partial \rho_e} \{\boldsymbol{\Theta}\}_e \tag{27}$$

We notice that employing a voxel mesh, all the elements are *geometrically congruent*. Further, on account of anisotropy and local variation in material property (thermal conductivity is expressed as a function of element density and element fiber orientation), the elements are not *behavioral congruent*. In the current work, we propose a formulation to exploit the geometrical congruency, and precompute the part of the stiffness matrix capturing the geometrical congruence and store them as templates. Then, on-the-fly, we only compute the

behavioral aspect of each element. This allows us to reduce the amount of computation considerably. To illustrate, we may express Equation 18 as

$$\frac{\partial [K]}{\partial \rho_e} = \iiint\limits_{\Omega_e} [B]^T \frac{\partial [k]_e}{\partial \rho_e} [B] d\Omega_e = \sum_{i=1}^{3} \sum_{j \geq i}^{3} \frac{\partial [k]_e^{ij}}{\partial \rho_e} \iiint\limits_{\Omega_e} [B]^T [\mathcal{J}]^{ij} [B] d\Omega_e = \sum_{i=1}^{3} \sum_{j \geq i}^{3} \frac{\partial [k]_e^{ij}}{\partial \rho_e} [K_{\mathcal{J}}]^{ij} \qquad (28)$$

Similarly, we may express Equation 20 as,

$$\frac{\partial [K]_e}{\partial \theta_e} = \sum_{i=1}^{3} \sum_{j \geq i}^{3} \frac{\partial [k]_e^{ij}}{\partial \theta_e} [K_{\mathcal{J}}]^{ij} \qquad (29)$$

Similar expression follows for sensitivity of the constraint with respect to the build plane orientation angles α_0 and β_0.

$[\mathcal{J}]^{ij} \in \mathcal{R}^{3\times3}$ is a matrix with a value of 1 at (i,j), (j,i) and 0 elsewhere. Note that the thermal conductivity tensor $[k] \in \mathcal{R}^{3\times3}$ is symmetric. This results in a total of $\frac{3\times4}{2} = 6$ distinctive entries, i.e., a total of six templates. The matrices $[K_{\mathcal{J}}]^{ij} \in \mathcal{R}^{8\times8}$ are pre-computed and stored as templates. During the computation of the solution, only the expressions given in Equations 19 and 21 (and likewise for $\frac{\partial [k]_e}{\partial \alpha_0}$ and $\frac{\partial [k]_e}{\partial \beta_0}$) are computed and are multiplied as scalars with the pre-computed templates. This illustrates the separation of geometric congruence withing the mesh and elements from the behavioral incongruous. This reduces the computational cost as a matrix of reduced size (here 3×3) is computed instead of the full stiffness matrix (here 8×8) for every element. Finally it is important to note that this combined with the assembly free-framework can be accelerated with fine-grain parallelization.

The matrix system in Equation 9 is usually solved in an iterative fashion, with the conjugate-gradient (CG) method being the common method. Various techniques are utilized to accelerate the convergence of the system. The current formulation uses physics based deflation adapted to solve thermal systems from [41] to accelerate the convergence of the conjugate-gradient solver. The concept of deflation was introduced in [29]. The idea is to construct a matrix referred to as the *deflation space*, whose columns approximately span the low eigenvectors of the effective stiffness matrix using agglomeration techniques. The method was illustrated in conjunction with the assembly-free method by [22] to solve structural dynamics physics. A sharp decrease in the number of conjugate-gradient iterations to solve the system is observed and is reported in section 4.4. The current work adapts this formulation for thermal system and also extends to consider the case where the elements don't exhibit behavorial congruence. The system is further accelerated using a Jacobi-preconditioner [28] which is a common practice to improve the condition number of the effective stiffness matrix.

4 Numerical Experiments

We now demonstrate the proposed method through several examples. The examples considered, and the corresponding sub-sections, are summarized in Table 2. For example, in sub-section 4.1.1, we optimize just the infill, by assuming a fixed build direction and fiber orientation. Similarly, in sub-section 4.1.2, we optimize just the fiber orientation, by assuming a fixed build direction, and fixed infill, and so on.

Section	Build Dir	Fiber Orient.	Infill
4.1.1	×	×	✓
4.1.2	×	✓	×
4.1.3	×	✓	✓
4.2	✓	×	✓
4.3	✓	✓	✓

Table 2: Summary of various examples considered

The computational performance is then summarized in Section 4.4.

4.1 Fixed Build Orientation

In this section, the build orientation is assumed to be fixed, while the infill and/or the fiber orientation is optimized.

4.1.1 Infill Optimization

Consider a three-dimensional plate, with a thickness of 0.5mm, illustrated in Figure 3. The thermal boundary conditions apply across the thickness as illustrated in Figure 3 where $T = 0°C$ and the heat flux $Q = 10^4 \, \text{W}/m^2$. The build direction is assumed to be fixed along the thickness direction. Further, the material is assumed to be isotropic with $k = 0.77$ [W/m-K], and therefore the fiber orientation is also not a design variable. The only design variable is the infill topology; the thermal compliance must be minimized for a target volume fraction of 0.5. For finite element analysis, the domain is discretized into 10^5 voxels, with one layer across the thickness.
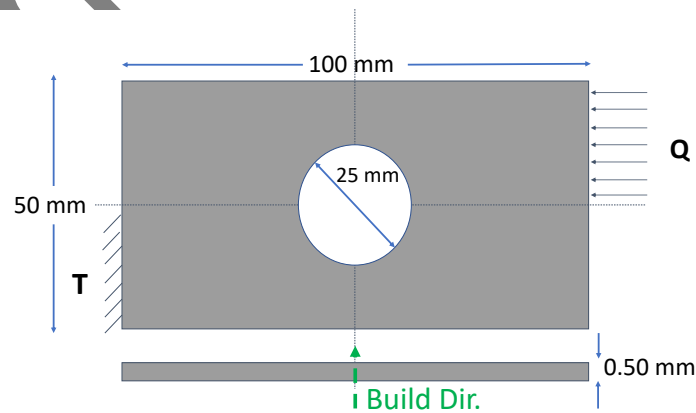
Figure 3: Illustration of a plate problem with thermal boundary conditions.

To optimize the infill, all elements are assigned a density of 0.5 (the target volume fraction). The optimization algorithm described earlier is now exploited to find the optimal infill topology that minimizes the thermal compliance. The optimization terminates when the relative change in the thermal compliance is less than 10^{-4}. The convergence is illustrated in Figure 4, together with the optimal infill topology. The units for compliance is Joules. Observe that the topology aligns with the flow of heat, as expected.
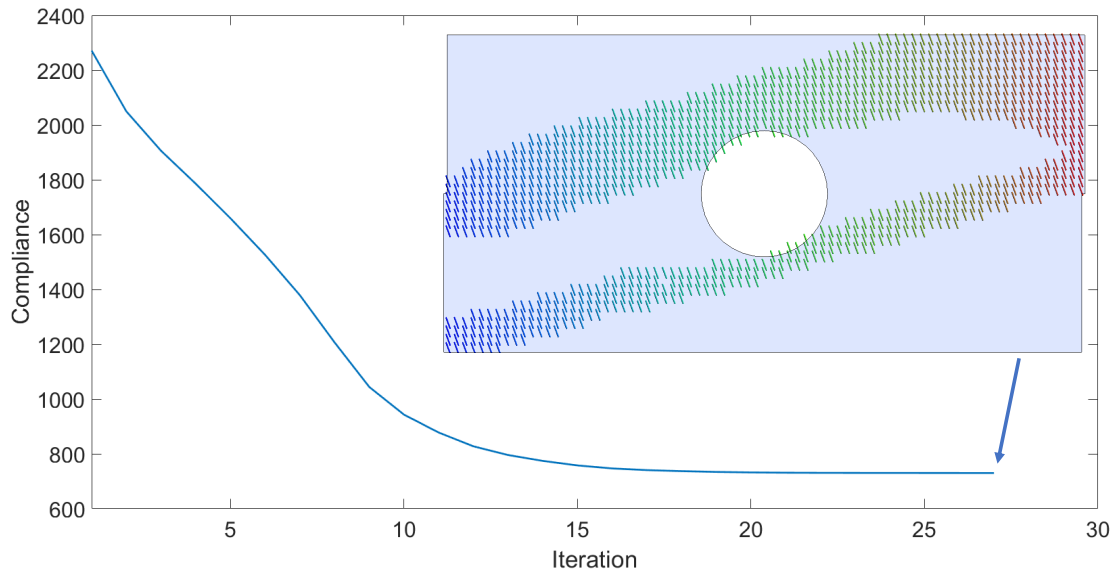

Figure 4: Optimization of infill topology.

4.1.2 Fiber Optimization

Next, we consider optimizing just the fiber orientation for the above example. Specifically, the material is assumed to be *PA6-CuF-25* (see Table 1). The anisotropic conductivity is an impetus for preferential fiber orientation. The build direction is fixed as before, and the infill is also fixed at 100%. All elements are initially oriented with $\theta_e = 0°$. After optimization, Figure 5 illustrates the orientation of the fibers obtained; this is consistent with expectations.
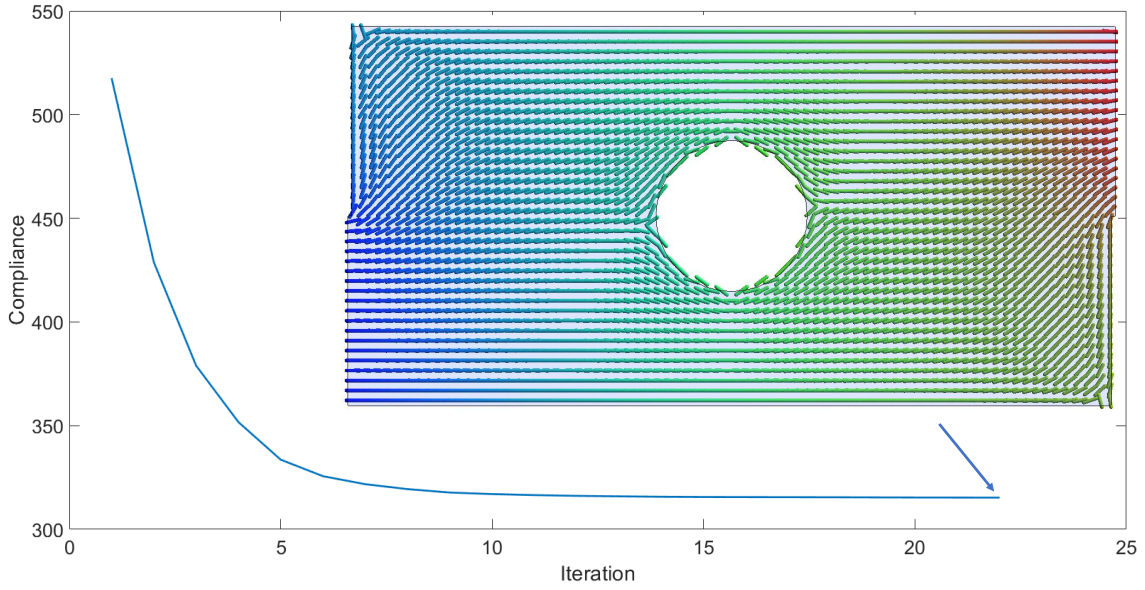
Figure 5: Optimization of fiber orientation.

4.1.3 Infill and Fiber Optimization

Next, we combine fiber and infill optimization for the same example. All elements have an initial density of 0.5, and the fibers are oriented at $\theta = 0°$. Figure 6 illustrates the convergence, and the resulting topology, with fiber orientation. We observe a significant improvement in performance in comparison to only optimizing the infill (section 4.1.1) or the fibers (section 4.1.2). The histogram in Figure 7(a) captures the distribution of fiber orientation.
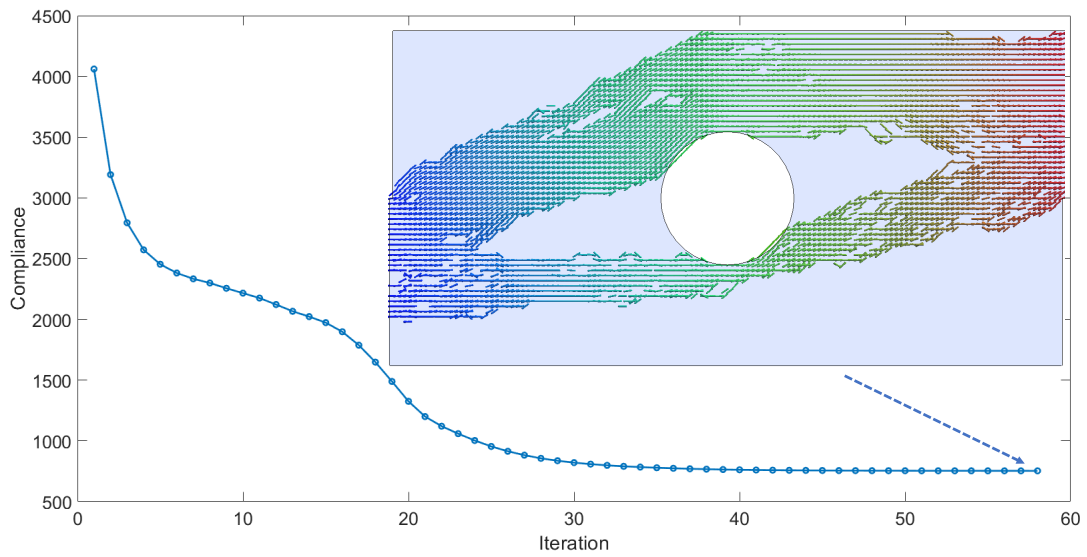
Figure 6: Optimization of infill topology and fiber orientation.

13

Figure 7(b) illustrates the final density distribution; the penalization ensures that the densities take extremal values.
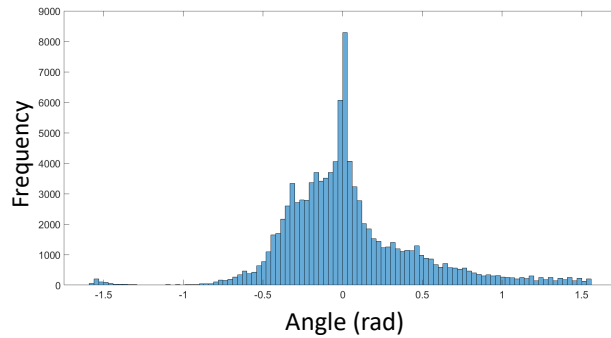
(a) The histogram of the fiber orientation angles θ_e upon optimization.
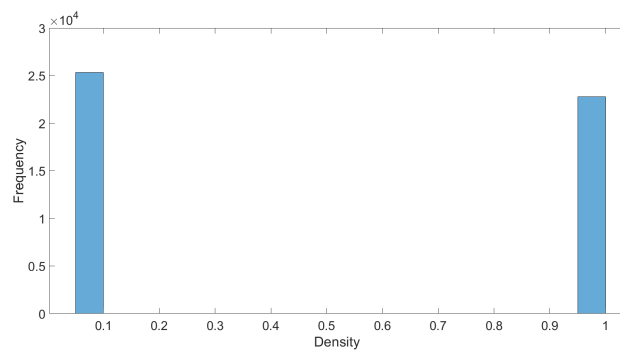
(b) The histogram of densities ρ_e upon optimization.

Figure 7: Distribution of Optimized variables.

4.2 Build Orientation and Infill Optimization

We now illustrate an example where the benefits of optimizing the build direction becomes evident. Consider the geometry shown in Figure 8 with $T = 0^\circ C$ on the top face, and a heat flux of 10^3 W$/m^2$ on the bottom face. The material is assumed to be isotropic, i.e., fiber orientation is disregarded. However, observe that depending on the build direction, inter-layer anisotropy will be induced. For example, if the build direction is along Z-axis, then $k_\parallel = k_\perp = 0.76$ [W/m-K] while $k_z = 0.45$ [W/m-K]. For finite element analysis, the domain was meshed with 100,000 voxels.
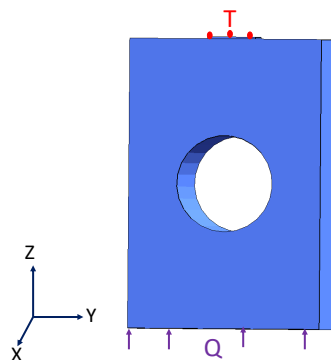
Figure 8: A cuboidal geometry with a center hole and the associated boundary conditions.

14

To isolate the impact of build direction, two sets of optimization studies were carried out. In the first set, the build direction was fixed along Z-axis; observe that this is sub-optimal since the heat sink and source are separated along the Z-axis. The infill was then optimized for 3 different volume fractions- 30%,50% and 75%. The final topology and compliance are reported in the second column of Table 3. In the second set, the build-direction was also optimized (with an initial guess along Z-axis). The resulting topology and thermal compliance, together with the optimal build-direction are reported in the third column. As one can observe, the compliance reduces significantly when the build direction is optimized; in each case, the optimal build direction is approximately along X-axis.
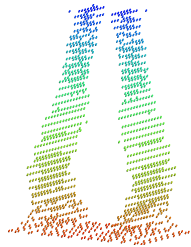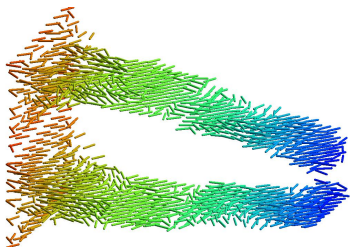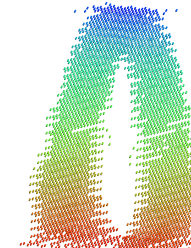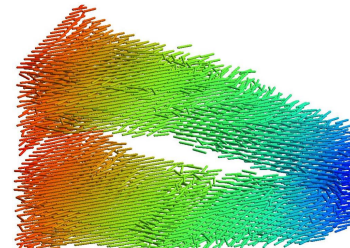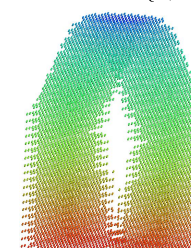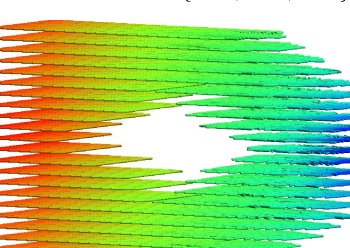
Volume Fraction (%)	Fixed Build Dir.	Optimized Build Dir.
30	C = 13.20 $\vec{b} = \{0, 0, 1\}$	C = 4.54 $\vec{b} = \{0.97, 0.21, 0.12\}$
50	C = 4.33 $\vec{b} = \{0, 0, 1\}$	C = 1.56 $\vec{b} = \{0.97, 0.22, 0.08\}$
75	C = 2.42 $\vec{b} = \{0, 0, 1\}$	C = 1.00 $\vec{b} = \{0.97, 0.22, 0.08\}$

Table 3: Infill optimization, with and without build direction optimization.

4.3 Complete Optimization

In this section, we highlight the full potential of the solver by simultaneously optimizing the infill topology, the fiber orientation and the build direction, for the geometry illustrated in Figure 9 . The prescribed boundary conditions are a fixed temperature of $0°C$ and a heat flux of 10^4 [W/m^2] on the tip of the rocker arm and a flux of 5×10^4 [W/m^2] on the circular face. We assume the material be *PA6-CuF-25* (table 1) with $k_z = 0.45$ [W/m-K]. The desired volume fraction is 0.5. The design is discretized with 50,000 voxels. As before, the initial density of all the elements is 0.5, the orientation of the fibers is $0°$, the initial build direction is along the X axis.

We plot the convergence of the objective in Figure 10. The plot shows the topology at various instances of the optimization process with the build vector at that instance. We observe a sharp decrease in the compliance between the first and second iteration. The example was chosen to exaggerate the effect of build orientation. A sharp gradient in the build orientation design variable guides the initial behavior of the optimizer. Observe that the optimizers considers various orientations to finally arrive at the optimal; an almost 10-fold decrease in compliance is observed.
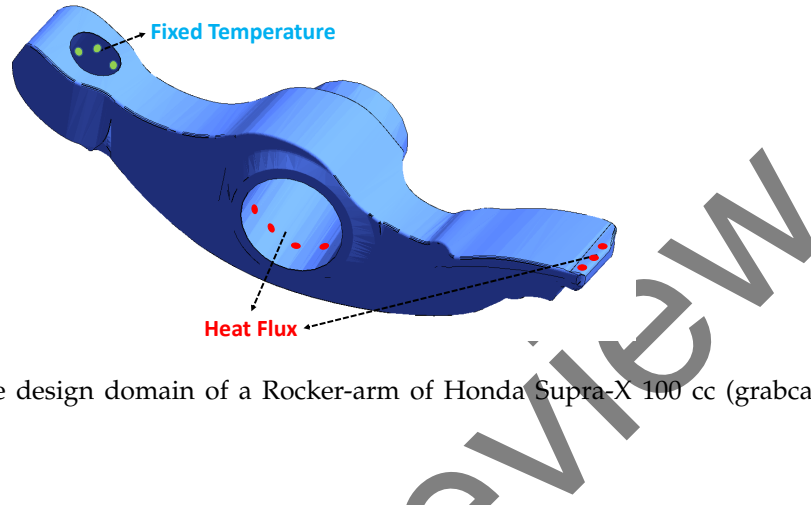

Figure 9: Illustration of the design domain of a Rocker-arm of Honda Supra-X 100 cc (grabcad.com) with boundary conditions.
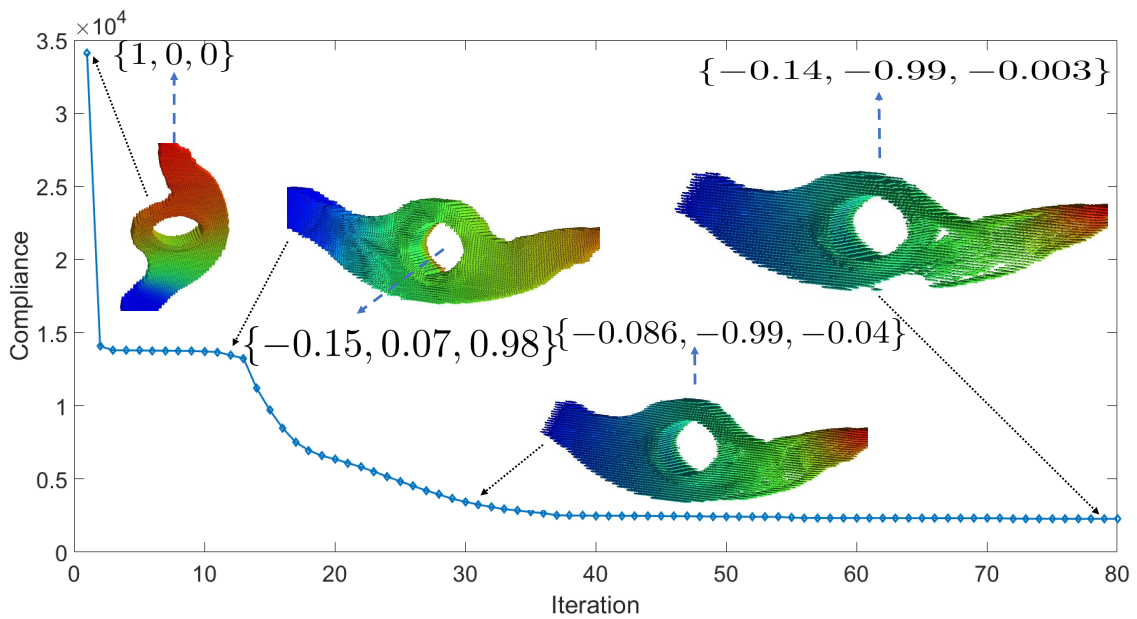

Figure 10: Plot of compliance with build direction.

4.4 Performance

All experiments were conducted on a desktop PC equipped with an Intel-i7 12-core processor with 32 GB RAM running at 3.2 GHz. Table 4 reports the time taken, and the number of optimization iterations required to solve various problems discussed above. In addition, the ratio between the final to initial compliance is reported to gauge the ratio of computational effort to performance improvement derived.

Section	#Elems	#Iter	Total time [min]	C_f/C_0
4.1.1	1e5	27	6.14	0.28
4.1.2	1e5	32	23.3	0.31
4.1.3	1e5	57	38.1	0.10
4.2 (fixed build; $V_f = 0.5$)	1e5	27	6.7	0.30
4.2 (opt build; $V_f = 0.5$)	1e5	78	110.3	0.08
4.3	5e4	80	75.8	0.05

Table 4: Performance statistics for different models

Further, it was observed that the solver spent 75% to 85% of time in solving the finite element system. To this end, as discussed, we employ a Jacobi preconditioner and physics based deflation as discussed earlier to accelerate the convergence. The effect of this can be seen in Table 5. To conduct this benchmark study, we solve the problem illustrated in Figure 8 with boundary conditions as prescribed. A voxel mesh with 5×10^4 elements was employed. We see a speed-up of 7 is achieved by employing the accelerators, thus cementing their value in achieving faster results.

Preconditioner	Deflation	# CG Iter	Time/FEM iter [s]
$\times$	$\times$	283	18.04
$\checkmark$	$\times$	260	16.62
$\times$	$\checkmark$	21	2.74
$\checkmark$	$\checkmark$	19	2.55

Table 5: Timing results for various solver configurations.

5 Conclusion

The main contribution of this paper is an integrated framework for the simulataneously optimization of the build direction, infill topology with the raster fiber orientation of SFRP components. A global volume constraint was imposed to drive the optimizer towards minimizing compliance. The layer-wise printing paradigm of AM was of central focus and methods were proposed to mitigate the consequence of the anisotropic material characterization. Further, the numerical experiments demonstrated that one may leverage fiber orientation to reap maximum benefit.

A limitation of FDM is the need for support material extending from the build plate. The present formulation optimizes the infill for improved functional performance but provides no guarantee that the infill design is self supporting. Also, the optimization of build orientation takes only the effect of material anisotropy, and does not consider its impact on sacrificial support. Constraints such as minumum feature size, surface finish, overhang surfaces, enclosed voids have not been considered in the formulation. Further post-processing might be required to produce smooth transitions in fiber orientation. Some of these limitations will be addressed in future work.

Acknowledgments

References

[1] M P Bendsoe and Ole. Sigmund. *Topology optimization: theory, methods, and applications*. Springer Berlin Heidelberg, 2 edition, 2003.

[2] A. Boschetto and L. Bottini. Accuracy prediction in fused deposition modeling. *The International Journal of Advanced Manufacturing Technology*, 73(5-8):913–928, Jul 2014.

[3] E. C. Botelho, Figiel, M. C. Rezende, and B Lauke. Mechanical behavior of carbon fiber reinforced polyamide composites. *Composites Science and Technology*, 63(13):1843–1855, Oct 2003.

[4] Christopher J Brampton, K Chauncey Wu, and H Alicia Kim. New optimization method for steered fiber composites using the level set method. *Structural and Multidisciplinary Optimization*, 52(3):493–505, 2015.

[5] Bastian Brenken, Eduardo Barocio, Anthony Favaloro, Vlastimil Kunc, and R. Byron Pipes. Fused filament fabrication of fiber-reinforced polymers: A review, may 2018.

[6] Laurent Chougrani, Jean Philippe Pernot, Philippe Véron, and Stéphane Abed. Lattice structure lightweight triangulation for additive manufacturing. *CAD Computer Aided Design*, 90:95–104, sep 2017.

[7] Charles Dapogny, Rafael Estevez, Alexis Faure, Georgios Michailidis, C Dapogny, R Estevez, A Faure, and Michailidis. Shape and topology optimization considering anisotropic features induced by additive manufacturing processes. *HAL Archives*, (hal01660850v2):1–39, 2018.

[8] Paramita Das, Ramya Chandran, Rutuja Samant, and Sam Anand. Optimum Part Build Orientation in Additive Manufacturing for Minimizing Part Errors and Support Structures. In *Procedia Manufacturing*, volume 1, pages 343–354. Elsevier, Jan 2015.

[9] Joshua D Deaton and Ramana V Grandhi. A survey of structural and multidisciplinary continuum topology optimization: post 2000. *Structural and Multidisciplinary Optimization*, 49(1):1–38, 2014.

[10] Shiguang Deng and Krishnan Suresh. Multi-constrained topology optimization via the topological sensitivity. *Structural and Multidisciplinary Optimization*, 51(5):987–1001, may 2015.

[11] Arghavan Farzadi, Mehran Solati-Hashjin, Mitra Asadi-Eydivand, and Noor Azuan Abu Osman. Effect of layer thickness and printing orientation on mechanical properties and dimensional accuracy of 3D printed porous samples for bone tissue engineering. *PLoS ONE*, 9(9):e108252, 2014.

[12] Miguel Fernandez-Vicente, Wilson Calle, Santiago Ferrandiz, and Andres Conejero. Effect of Infill Parameters on Tensile Mechanical Behavior in Desktop 3D Printing. *3D Printing and Additive Manufacturing*, 3(3):183–192, Sep 2016.

[13] T Gao, W H Zhang, J H Zhu, Y J Xu, and D H Bassir. Finite Elements in Analysis and Design Topology optimization of heat conduction problem involving design-dependent heat load effect. *Finite Elements in Analysis and Design*, 44:805–813, 2008.

[14] Allan Gersborg-Hansen, Martin P Bendsøe, and Ole Sigmund. Topology optimization of heat conduction problems using the finite volume method. *Structural and multidisciplinary optimization*, 31(4):251–259, 2006.

[15] I. Gibson, D. W. Rosen, and B. Stucker. *Additive manufacturing technologies: Rapid prototyping to direct digital manufacturing*. Springer, New York, 2010.

[16] Thomas J.R. Hughes, Itzhak Levit, and James Winget. An element-by-element solution algorithm for problems of structural and solid mechanics. *Computer Methods in Applied Mechanics and Engineering*, 36(2):241–254, Feb 1983.

[17] F Knoop and V Schoeppner. Mechanical and Thermal Properties of Fdm Parts Manufactured With Polyamide 12. *Solid Freeform Fabrication Symposium*, pages 935–948, 2015.

[18] Anirudh Krishnakumar, Krishnan Suresh, and Aaditya Chandrasekhar. Towards Assembly-Free Methods for Additive Manufacturing Simulation. In *Volume 1A: 35th Computers and Information in Engineering Conference*, page V01AT02A021. ASME, Aug 2015.

[19] Qing Li, Grant P. Steven, Osvaldo M. Querin, and Y. M. Xie. Shape and topology design for heat conduction by Evolutionary Structural Optimization. *International Journal of Heat and Mass Transfer*, 42(17):3361–3371, Sep 1999.

[20] Jonàs Martínez, Jérémie Dumas, and Sylvain Lefebvre. Procedural Voronoi Foams for Additive Manufacturing. *ACM Transactions on Graphics*, 35(4):12, Jul 2016.

[21] Amir M. Mirzendehdel, Behzad Rankouhi, and Krishnan Suresh. Strength-based topology optimization for anisotropic parts. *Additive Manufacturing*, 19:104–113, Jan 2018.

[22] Amir M. Mirzendehdel and Krishnan Suresh. A Deflated Assembly Free Approach to Large-Scale Implicit Structural Dynamics. *Journal of Computational and Nonlinear Dynamics*, 10(6):061015, Nov 2015.

[23] Omar A Mohamed, Syed H. Masood, and Jahar L Bhowmik. Optimization of fused deposition modeling process parameters: a review of current research and future prospects. *Advances in Manufacturing*, 3(1):42–53, 2015.

[24] Thomas Mulholland, A Falke, and Natalie Rudolph. Filled Thermoconductive Plastics for Fused Filament Fabrication. In *Solid Freeform Fabrication*, pages 871–883, Austin, TX, 2016.

[25] A Sanati Nezhad, F Barazandeh, A R Rahimi, and M Vatani. Pareto-Based Optimization of Part Orientation in Stereolithography. *Proceedings of the Institution of Mechanical Engineers, Part B: Journal of Engineering Manufacture*, 224(10):1591–1598, Oct 2010.

[26] Hardikkumar Prajapati, Darshan Ravoori, Robert L. Woods, and Ankur Jain. Measurement of anisotropic thermal conductivity and inter-layer thermal contact resistance in polymer fused deposition modeling (FDM). *Additive Manufacturing*, 21:84–90, May 2018.

[27] Xiaoping Qian. Undercut and overhang angle control in topology optimization: A density gradient based integral approach. *International Journal for Numerical Methods in Engineering*, 111(3):247–272, jul 2017.

[28] Yousef Saad and Henk A. van der Vorst. Iterative solution of linear systems in the 20th century. *Journal of Computational and Applied Mathematics*, 123(1-2):1–33, Nov 2000.

[29] Yousef Saad, M. Yeung, J. Erhel, and F. Guyomarc'h. A deflated version of the conjugate gradient algorithm. *SIAM Journal on Scientific Computing*, 21(5):1909–1926, Jan 2000.

[30] Ole Sigmund. A 99 line topology optimization code written in matlab. *Structural and multidisciplinary optimization*, 21(2):120–127, 2001.

[31] Ole Sigmund and Kurt Maute. Topology optimization approaches. *Structural and Multidisciplinary Optimization*, 48(6):1031–1055, 2013.

[32] J. Stegmann and E. Lund. Discrete material optimization of general composite shell structures. *International Journal for Numerical Methods in Engineering*, 62(14):2009–2027, Feb 2005.

[33] John C. Steuben, Athanasios P. Iliopoulos, and John G. Michopoulos. Implicit slicing for functionally tailored additive manufacturing. *Computer-Aided Design*, 77:107–119, aug 2016.

[34] Krister Svanberg. The method of moving asymptotesa new method for structural optimization. *International journal for numerical methods in engineering*, 24(2):359–373, 1987.

[35] Erva Ulu, Emrullah Korkmaz, Kubilay Yay, O. Burak Ozdoganlar, and Levent Burak Kara. Enhancing the Structural Performance of Additively Manufactured Objects Through Build Orientation Optimization. *Journal of Mechanical Design*, 137(11):111410–1—-111410–9, Oct 2015.

[36] Nobuyuki Umetani and Ryan Schmidt. Cross-sectional structural analysis for 3D printing optimization. In *SIGGRAPH Asia 2013 Technical Briefs on - SA '13*, pages 1–4, New York, New York, USA, 2013. ACM Press.

[37] Wikipedia contributors. Fused filament fabrication — Wikipedia, the free encyclopedia, 2018. [Online; accessed 25-May-2018].

[38] Jun Wu, Niels Aage, Ruediger Westermann, and Ole Sigmund. Infill Optimization for Additive Manufacturing – Approaching Bone-like Porous Structures. *IEEE Transactions on Visualization and Computer Graphics*, 24(2):1127–1140, 2018.

[39] Jun Wu, Anders Clausen, and Ole Sigmund. Minimum compliance topology optimization of shellinfill composites for additive manufacturing. *Computer Methods in Applied Mechanics and Engineering*, 326:358–375, Nov 2017.

[40] Praveen Yadav and Krishnan Suresh. Assembly-Free Large-Scale Modal Analysis on the Graphics-Programmable Unit. *Journal of Computing and Information Science in Engineering*, 13(1):011003, Jan 2013.

[41] Praveen Yadav and Krishnan Suresh. Large Scale Finite Element Analysis via Assembly-Free Deflated Conjugate Gradient. *Journal of Computing and Information Science in Engineering*, 14(4):041008, Oct 2014.

[42] Pu Zhang, Jikai Liu, and Albert C. To. Role of anisotropic properties on topology optimization of additive manufactured load bearing structures. *Scripta Materialia*, 135:148–152, Jul 2017.